PIER C

(Received 12 January 2026, Accepted 10 February 2026, Scheduled 18 March 2026)

Slot-Loading-Enabled Compact UWB Planar Antenna with Circuit-Backed Modelling and Design for Defense Communication

Sonal Dubal[1,*], Hetal Pathak[2], and Vikas Gupta[3]

[1] *Faculty of Electronics and Communication Engineering, Parul University, Waghodia, Vadodara, Gujarat, India*
[2] *Electronics and Communication Engineering, Parul Institute of Technology, Parul University, Vadodara, Gujarat, India*
[3] *Electronics and Telecommunication Engineering, Vidyavardhini's College of Engineering and Technology, Maharashtra, India*

ABSTRACT: This paper proposes a slot-loading-enabled compact ultra-wideband (UWB) planar antenna supported by circuit-backed modelling that targets defense communication systems. The antenna was realized on a compact footprint of $10\times 12\times 1.5$ mm^3, corresponding to an electrical size of approximately $0.29\lambda\times 0.35\lambda\times 0.043\lambda$ at the center frequency. Through the combined use of a modified circular radiator, strategically introduced slots, a stepped feed network, and a defected ground plane, the antenna achieves a continuous impedance bandwidth from 2.4 to 15 GHz. This corresponds to an absolute bandwidth of 12.6 GHz, a fractional bandwidth of nearly 145%, and a center frequency of 8.7 GHz, confirming the UWB operation. The antenna attains a maximum gain of 6.37 dB with a radiation efficiency reaching 89%. Stable radiation characteristics were observed, with dominant co-polarized fields and well-suppressed cross-polarization in both the principal planes. An electrical equivalent circuit provides physical insight into the multi-resonant behavior and enables efficient circuit-level validation. The measured results were in close agreement with the simulations, demonstrating the suitability of the antenna for compact UWB defense communication applications.

1. INTRODUCTION

Microstrip patch antennas have attracted significant attention in modern wireless communication systems because of their low profile, light weight, ease of fabrication, and compatibility with planar circuitry. However, conventional microstrip antennas inherently suffer from a narrow impedance bandwidth and limited gain, which restrict their applicability in emerging wide-band and high-frequency systems. Consequently, extensive research efforts have been directed toward improving antenna bandwidth, radiation efficiency, and polarization characteristics through innovative geometries, slot loading, parasitic elements, and ground-plane modifications [1].

With the rapid evolution of fifth-generation (5G), millimeterwave (mmWave), and beyond-5G communication systems, antennas capable of operating over wide and multi-band frequency ranges have become essential. Several broadband and mmWave microstrip antenna designs have been reported for 5G applications, particularly around the 28 GHz and higher frequency bands [2–4]. Slot-loaded U-shaped patch antennas with partial ground planes have demonstrated enhanced bandwidth and dual-beam radiation characteristics, making them suitable for high-data-rate wireless services [4, 5]. Wide-band antenna design techniques involving slot cuts, modified patch shapes, and defective structures have also been explored to improve impedance matching without significantly increasing antenna size [6–8].

Recent research has further emphasized the importance of compact and ultra-wideband (UWB) antennas to support diverse wireless standards, including microwave, mmWave, and future terahertz (THz) systems [9–11]. Slot-based and parasitic-loaded planar antennas have proven effective in achieving broadband behavior, improved polarization purity, and stable radiation patterns [12–14]. Compact planar antennas operating across the S, C, X, and microwave 5G bands have also been reported, highlighting the need for antenna structures that combine miniaturization with wide-band performance [15–19]. Despite these advancements, achieving continuous wide-band operation with stable impedance matching, low cross-polarization, and high radiation efficiency using a compact planar configuration remains a challenge.

Motivated by these requirements, the present work proposes a compact planar antenna that incorporates a modified circular radiator, slot loading, a stepped feed structure, and defective ground plane to achieve wide-band operation. The antenna was designed to achieve stable impedance matching, enhanced bandwidth, and efficient radiation, making it suitable for modern wide-band and multi-frequency wireless applications.

The remainder of this paper is organized as follows. First, the graphical abstract summarizes the overall design, fabrication, and measurement workflow of the proposed antenna. The following section describes the antenna geometry and design considerations, followed by the evolution of the antenna structure for bandwidth enhancement. Electrical equivalent circuit modelling and parametric analysis are then presented to explain

* Corresponding author: Sonal Dubal (sonaldubal468@gmail.com).

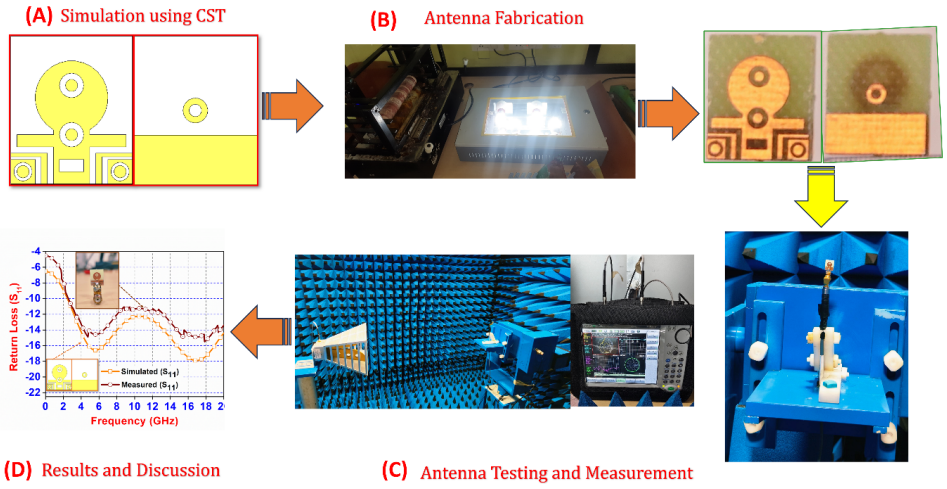

FIGURE 1. Graphical overview of antenna design, fabrication, measurement, and validation process.

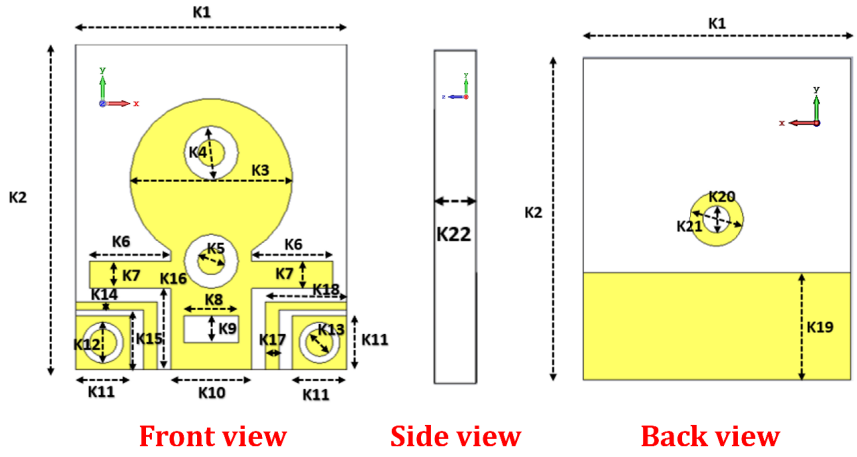

FIGURE 2. Front, side, and back views of the proposed planar antenna with dimensional parameters.

antenna behavior. Finally, simulated and measured results are discussed to validate the performance of the proposed antenna.

2. GRAPHICAL ABSTRACT

Figure 1 illustrates a graphical abstract summarizing the complete development workflow of the proposed planar antenna, from numerical design to experimental verification. In stage (A), the antenna geometry was modeled and optimized using full-wave electromagnetic simulations in Computer Simulation Technology (CST) Microwave Studio, where both the radiating element and ground-plane features were examined to achieve wide-band impedance matching. Based on the optimized parameters, stage (B) depicts the fabrication of the antenna on an FR-4 substrate using standard printed circuit board (PCB) fabrication processes, ensuring the accurate realization of the slot-loaded radiator, feed network, and ground-plane structure.

The subsequent stages emphasize the experimental validation and performance assessment. In stage (C), the fabricated antenna was evaluated inside an anechoic chamber using a vector network analyzer (VNA) to measure the reflection characteristics and radiation performance under controlled conditions. Finally, stage (D) presents the results and discussion, in which the measured responses are compared with simulated data. The strong agreement between the simulation and experiment verifies the effectiveness of the proposed design approach and confirms the suitability of the antenna for wideband and defense communication applications.

3. ANTENNA GEOMETRY AND DESIGN METHODOLOGY

Figure 2 illustrates the geometry of the proposed planar antenna, where the front view presents a compact rectangular configuration defined by the overall dimensions K_1 and K_2. A modified circular radiating patch was centrally positioned on the substrate, and its effective size was governed by K_3. An internal circular slot (K_4) is etched within the patch to introduce capacitive loading, which aids in resonance tuning and impedance matching. An additional circular slot near the feed junction (K_5) improved the electromagnetic coupling between the feed line and the radiator.

TABLE 1. Dimensional parameters of the proposed planar antenna.

PARAMETER	VALUE (in mm)	PARAMETER	VALUE (in mm)
K1	10	K12	1.5
K2	12	K13	1
K3	6	K14	0.3
K4	2	K15	2.2
K5	1	K16	3
K6	3	K17	0.5
K7	1	K18	3
K8	2	K19	4
K9	1	K20	1
K10	3	K21	2
K11	2	K22	1.5

The antenna is excited through a stepped and slotted microstrip feed structure, in which the dimensions K_6–K_{18} function as impedance-transforming sections and matching elements. Supplementary rectangular and circular slots near the lower region modify the surface current distribution, suppress undesired resonant modes, and support wide-band operation while preserving the structural symmetry.

The side and back views describe the substrate and ground-plane features of the antenna. The side view emphasizes a thin dielectric substrate with uniform thickness K_{22}, confirming a low-profile planar structure suitable for compact radio frequency (RF) applications. The back view shows a partial ground plane extending to K_{19}, which enhances the bandwidth by altering the return current path. A circular slot etched in the ground plane, defined as K_{20} and K_{21}, forms a defective ground structure that introduces additional inductive and capacitive effects. The combined action of the partial ground plane and defective structure results in improved impedance bandwidth, controlled resonance behavior, and stable radiation performance across the operating frequency range.

The geometric parameters listed in Table 1 precisely define the compact planar antenna structure and enable controlled electromagnetic behavior. The overall antenna size was governed by $K_1 = 10\,\text{mm}$ and $K_2 = 12\,\text{mm}$, which set the length and width of the substrate, respectively. The main circular radiating patch is characterized by $K_3 = 6\,\text{mm}$, whereas the inner circular slot of the radiator, defined by $K_4 = 2\,\text{mm}$, introduces reactive loading to shift and stabilize the resonant frequencies. A smaller circular slot near the feed region ($K_5 = 1\,\text{mm}$) improves the electromagnetic coupling between the feedline and radiator. The feed transition and lateral extensions are controlled by $K_6 = 3\,\text{mm}$ and $K_7 = 1\,\text{mm}$, which act as impedance-matching sections to ensure an efficient power transfer across a wide frequency range.

The lower portion of the antenna consists of several finely tuned features that enhance bandwidth and current distribution. The parameters $K_8 = 2\,\text{mm}$ and $K_9 = 1\,\text{mm}$ define a rectangular slot that modifies the surface current path, whereas $K_{10} = 3\,\text{mm}$ and $K_{11} = 2\,\text{mm}$ determine the horizontal extent of the bottom section. The etched circular slots located symmetrically at the lower corners were defined by $K_{12} = 1.5\,\text{mm}$ and $K_{13} = 1\,\text{mm}$, contributing to resonance control and radiation stability. Narrow slots and steps defined by $K_{14} = 0.3\,\text{mm}$, $K_{15} = 2.2\,\text{mm}$, $K_{16} = 3\,\text{mm}$, $K_{17} = 0.5\,\text{mm}$, and $K_{18} = 3\,\text{mm}$ further refine impedance matching by introducing gradual discontinuities. On the ground plane, $K_{19} = 4\,\text{mm}$ specifies the partial ground height, whereas the defected ground structure is governed by $K_{20} = 1\,\text{mm}$ and $K_{21} = 2\,\text{mm}$, which perturb the return current path to enhance the bandwidth. Finally, the substrate thickness $K_{22} = 1.5\,\text{mm}$ confirms the low-profile nature of the antenna, making it suitable for compact and high-frequency wireless applications.

4. ELECTRICAL EQUIVALENT CIRCUIT MODELLING

The proposed planar antenna is modelled using an RF circuit representation of the proposed antenna, excited by a $50\,\Omega$ feed line as shown in Figure 3, where the radiating behavior is represented by three parallel RLC resonator branches corresponding to different physical sections of the antenna. The main circular patch is modelled by an RLC branch ($\approx 86\,\Omega$, 1.2 nH, 0.92 pF) and generates the fundamental resonance. The slot-loaded region is represented by a second RLC branch ($\approx 82\,\Omega$, 0.55 nH, 0.54 pF), which introduces additional capacitive loading and improves mid-band impedance matching. The lower stepped arms form the third RLC branch ($\approx 95\,\Omega$, 0.32 nH, 0.44 pF), which is responsible for higher-frequency resonance and bandwidth extension.

In addition, the defected ground structure (DGS) is modelled as a series LC network ($\approx 0.2\,\text{nH}$, 0.3 pF), which modifies the ground current path, suppresses unwanted modes, and enhances the impedance bandwidth. The combined response of these resonators accurately explains the observed multi-resonant and wide-band S_{11} behavior. Overall, the equivalent electrical circuit (EEC) provides a clear circuit-level interpretation of antenna operation and validates the wide-band performance achieved through radiator shaping, slot loading, and ground-plane defect parameters of the equivalent circuit model, mentioned in Table 2.

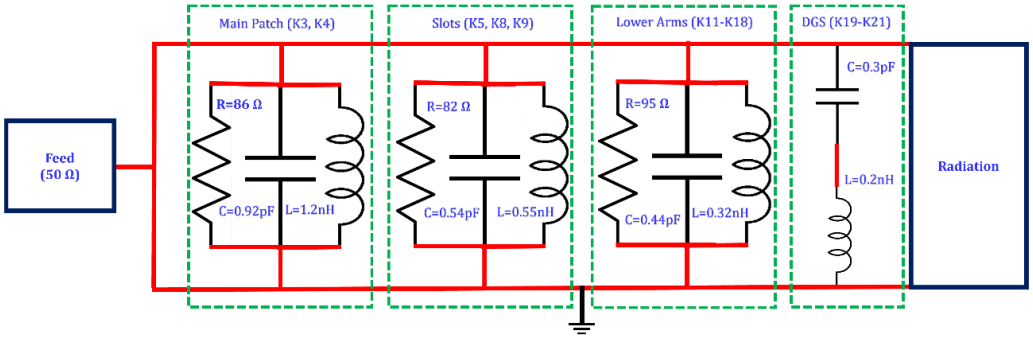

FIGURE 3. Equivalent RF circuit representation of the proposed antenna.

TABLE 2. Parameters of the equivalent circuit model.

Branch	R (Ω)	L (nH)	C (pF)	Physical Interpretation
$R_1L_1C_1$	∼86	1.2	0.92	Main circular patch
$R_2L_2C_2$	∼82	0.55	0.54	Slot coupling
$R_3L_3C_3$	∼95	0.32	0.44	Lower stepped arms
DGS		0.2	0.3	Ground defect

Resonant frequency

$$f_0 = \frac{1}{2\pi\sqrt{LC}} \tag{1}$$

Quality factor (from S_{11} bandwidth)

$$Q \approx \frac{f_0}{BW_{-10\,\mathrm{dB}}} \tag{2}$$

Parallel resistance

$$R \approx Q \cdot \omega_0 L \tag{3}$$

4.1. Resonator-1: Main Circular Patch (K_3, K_4)

The fundamental resonance of the proposed antenna is mainly produced by the main circular radiating patch. This resonance corresponds to the longest surface current path on the antenna and dominates the lower operating frequency band. The resonant frequency is identified from the measured S_{11} response as follows:

$$f_1 \approx 4.8\,\mathrm{GHz} \tag{4}$$

The equivalent inductance is selected based on the effective current loop formed on the circular patch and is estimated as follows:

$$L_1 \approx 1.2\,\mathrm{nH} \tag{5}$$

Using the standard resonance condition of a parallel RLC circuit, the equivalent capacitance is calculated as follows:

$$C_1 = \frac{1}{(2\pi f_1)^2 L_1} \approx 0.92\,\mathrm{pF} \tag{6}$$

The quality factor is estimated from the 10 dB impedance bandwidth ($BW \approx 2.0\,\mathrm{GHz}$) as

$$Q_1 \approx \frac{f_1}{\mathrm{BW}} = \frac{4.8}{2.0} \approx 2.4 \tag{7}$$

The corresponding equivalent resistance, representing radiation and ohmic losses, is obtained as

$$R_1 \approx Q_1\omega_1 L_1 \approx 86\,\Omega \tag{8}$$

This RLC branch effectively modeled the dominant surface current loop on the main circular patch and established the fundamental resonance of the antenna.

4.2. Resonator-2: SlotLoaded Region (K_5, K_8, K_9)

The second resonator corresponds to the slot-loaded region defined by the parameters $K5$, $K8$, and $K9$. The etched slots introduce additional capacitive loading and elongate the effective current path, resulting in higher-order resonance and improved impedance matching in the midfrequency band. The resonant frequency associated with this mode was observed at

$$f_2 \approx 9.2\,\mathrm{GHz} \tag{9}$$

Owing to the shorter electrical length than that of the main patch, a reduced inductance value is selected as,

$$L_2 \approx 0.55\,\mathrm{nH} \tag{10}$$

with the equivalent capacitance estimated as

$$C_2 \approx 0.54\,\mathrm{pF} \tag{11}$$

From the -10 dB impedance bandwidth ($BW \approx 3.5\,\mathrm{GHz}$), the quality factor is calculated as follows:

$$Q_2 \approx \frac{9.2}{3.5} \approx 2.6 \tag{12}$$

The equivalent resistance for this resonator is therefore

$$R_2 \approx 82\,\Omega \tag{13}$$

This resonator models mid-band resonance, where the slot structures act as reactive loading elements that enhance impedance matching and contribute to bandwidth broadening.

4.3. Resonator-3: Lower Stepped Arms (K_{11}-K_{18})

The third resonator represents the lower stepped arms of the antenna, defined by the parameters K_{11}–K_{18}. These compact structures support shorter current paths and generate high frequency resonance, thereby extending the antenna operation toward the upper frequency region. The corresponding resonant

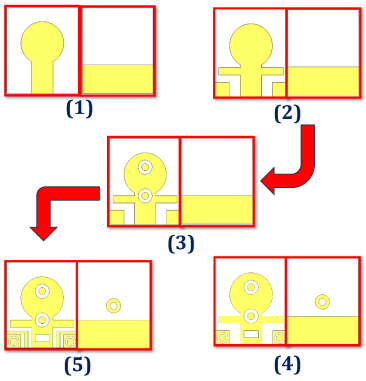

FIGURE 4. Evolution stages of the antenna geometry.

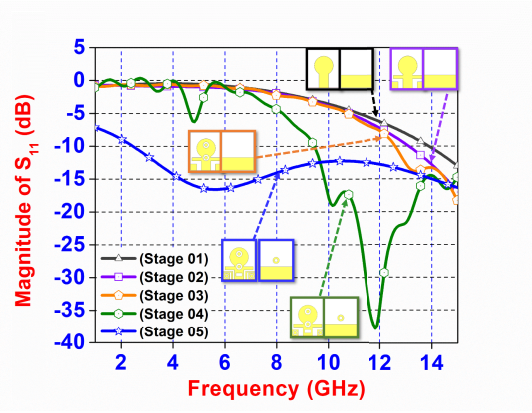

FIGURE 5. Simulated magnitude of (S_{11}) comparison for different antenna design stages.

frequency is identified as

$$f_3 \approx 13.5\,\text{GHz} \tag{14}$$

Owing to the reduced electrical length, the inductance is smaller and estimated as

$$L_3 \approx 0.32\,\text{nH} \tag{15}$$

while the equivalent capacitance is

$$C_3 \approx 0.44\,\text{pF} \tag{16}$$

Using the $-10\,\text{dB}$ bandwidth $(BW \approx 3.8\,\text{GHz})$, the quality factor is estimated as

$$Q_3 \approx \frac{13.5}{3.8} \approx 3.5 \tag{17}$$

The associated resistance is calculated as

$$R_3 \approx 95\,\Omega \tag{18}$$

This RLC branch accurately models the high-frequency resonance produced by compact lower stepped arms and contributes to the overall wide-band behavior of the antenna.

4.4. Defected Ground Structure (DGS) Modelling

In addition to the radiating elements, the defected ground structure (DGS) defined by parameters K_{19}–K_{21} was modelled as a series LC network. The DGS alters the ground-plane current distribution and introduces additional reactive loading, which suppresses the unwanted resonant modes and enhances the impedance bandwidth. From an equivalent-circuit perspective, the DGS behaves as a frequency-selective reactive element connected to the ground plane.

The inductive component arises from the elongated current path around the ground defect, whereas the capacitive component arises from the gap between the defective and intact ground regions.

4.5. Equivalent Circuit Parameters of the DGS

Based on the observed flattening of the S_{11} response and improved impedance matching, the extracted parameter ranges for the DGS are:

$$L_g = 0.15 - 0.25\,\text{nH} \tag{19}$$

$$C_g = 0.25 - 0.35\,\text{pF} \tag{20}$$

For circuit-level simulation and validation, the nominal values are selected as

$$L_g \approx 0.2\,\text{nH} \text{ and } C_g \approx 0.3\,\text{pF} \tag{21}$$

These values provide an effective tradeoff between the bandwidth enhancement and impedance stability across the operating frequency range. The radiation block at the output represents the conversion of guided electromagnetic energy into free-space radiation.

4.6. Physical Interpretation and Performance Impact

The inductance L_g represents the additional magnetic energy storage caused by the meandered current path around the ground-plane defect, which effectively lowers the resonant frequency without increasing the antenna size. Capacitance C_g models the electric-field coupling across the ground discontinuity and improves impedance matching by compensating for inductive reactance at higher frequencies.

4.6.1. Input Impedance Representation

The overall input impedance of the antenna can be expressed as

$$Z_{\text{in}} = Z_{\text{feed}} + \sum_{i=1}^{n} \frac{R_i}{1 + jQ_i\left(\frac{f}{f_i}\middle|\frac{f_i}{f}\right)}, \tag{22}$$

where each parallel $R_iL_iC_i$ branch corresponds to a distinct physical resonance of the antenna

5. DESIGN EVOLUTION AND IMPEDANCE ANALYSIS

Figure 4 illustrates the step-by-step evolution of the proposed planar antenna geometry, showing how each modification contributes to performance enhancement. In Stage (1), a simple circular radiating patch fed by a narrow microstrip line was introduced with a partial ground plane to establish the basic resonant behavior. Stage (2) adds horizontal extensions to the feed region, which increases the effective current path and improves the impedance matching while maintaining a compact structure.

In Stage (3), circular slots are etched into the main radiator and feed junction, creating additional resonant paths and enabling a multi-band operation. Stage (4) further refines the

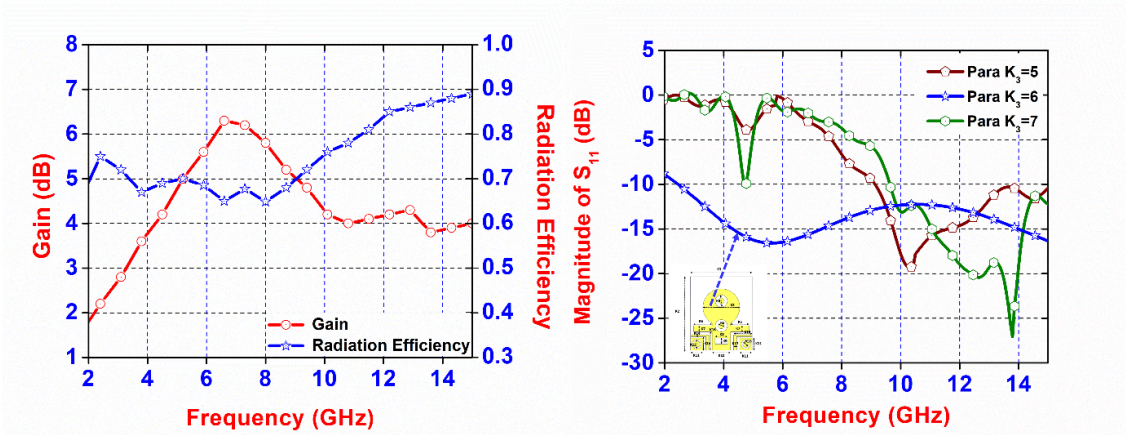

(a) (b)

FIGURE 6. (a) Gain and radiation efficiency variation with frequency and (b) Magnitude of (S_{11}) curve shows the effect of patch parameter K_3.

structure by introducing side slots and ground modifications, which enhance the bandwidth and stabilize the current distribution. Finally, Stage (5) incorporates stepped arms and corner slots, resulting in improved impedance bandwidth and resonance control. This progressive design approach clearly demonstrates how systematic geometric modifications can lead to a compact wide-band planar antenna.

The return-loss response shows a clear bandwidth enhancement as the antenna progresses through successive design stages, as shown in Figure 5. Stage (1) exhibits resonance only in the higher-frequency region, with acceptable impedance matching observed from 11.9 to 15 GHz, indicating limited operational bandwidth. With the introduction of additional structural features in Stage (2), the impedance bandwidth slightly improved and extended from 11 to 15 GHz, reflecting better coupling between the feed and the radiator.

In Stage (3), the further modification of radiating and slot regions shifts the lower cutoff frequency, resulting in an operating band from 10.8 to 15 GHz. Stage (4) shows a substantial enhancement in bandwidth, where strong resonances are achieved from 8 GHz to 15 GHz, confirming the effectiveness of the added slots and ground modifications. Finally, the final stage delivers wide-band performance, maintaining S_{11} below -10 dB over a broad frequency range from 2.4 to 15 GHz, demonstrating stable impedance matching and validating the optimized antenna design.

6. PARAMETRIC ANALYSIS OF SLOT AND GROUND STRUCTURES

In Figure 6(a), radiation characteristics indicate that the proposed antenna achieves a peak gain of 6.37 dB with a maximum radiation efficiency of approximately 89%, confirming efficient radiation over the operating band. The gain increases gradually with frequency, attaining its maximum value in the mid-to-high frequency region, while the efficiency remains consistently high, demonstrating low conduction and dielectric losses and stable radiation performance across the wide bandwidth.

In Figure 6(b), the parametric study of the main circular patch dimension $(K3)$ reveals its strong influence on impedance matching and resonant behavior. For $K3 = 5$, the antenna resonates mainly in the higher band, providing effective operation from 7.5 to 15 GHz. When $K3$ is increased to 6, the antenna exhibits wide-band behavior with a continuous resonant response from 2.5 to 15 GHz, indicating optimal coupling and bandwidth enhancement. For $K3 = 7$, the resonant response splits into two regions, with a narrow resonance around 4.5–5 GHz and a broader band extending from 9 to 15 GHz. These results confirm that the careful tuning of $K3$ is critical for achieving wide-band impedance matching and optimal antenna performance.

In Figure 7(a), the parametric analysis clearly shows the effect of $K5$ on the impedance bandwidth of the antenna. For $K5 = 0.5$, the antenna resonates only in the higher frequency region, providing effective operation from 7 to 15 GHz. When $K5$ is increased to 1, strong impedance matching is achieved over a much wider range, extending from 2.4 to 15 GHz, indicating optimal coupling between the feed and the radiating structure. Further increasing the parameter to $K5 = 1.5$ splits the resonance into two regions, with a narrow band around 4.5–5 GHz and a wide upper band from 9 to 15 GHz, due to excessive reactive loading near the feed.

In Figure 7(b), similarly, the variation of the ground-plane parameter K_{21} significantly influences the return-loss response. For $K_{21} = 1$, the antenna exhibits resonance mainly in the upper band from 9.8 to 15 GHz. When K_{21} is set to 2, the antenna achieves wide-band operation covering 2.4 to 15 GHz, confirming effective defected ground coupling and improved impedance matching. Increasing K_{21} to 3 shifts the resonance toward higher frequencies, resulting in operation from 10 to 15 GHz. These results demonstrate that the proper tuning of both K_5 and K_{21} is essential for achieving wide-band and stable antenna performance.

7. EXPERIMENTAL RESULTS AND DISCUSSION

Figure 8(a) illustrates a comparison between the simulated and measured return-loss (S_{11}) results, showing that the proposed antenna provides continuous wide-band operation from 2.4 to

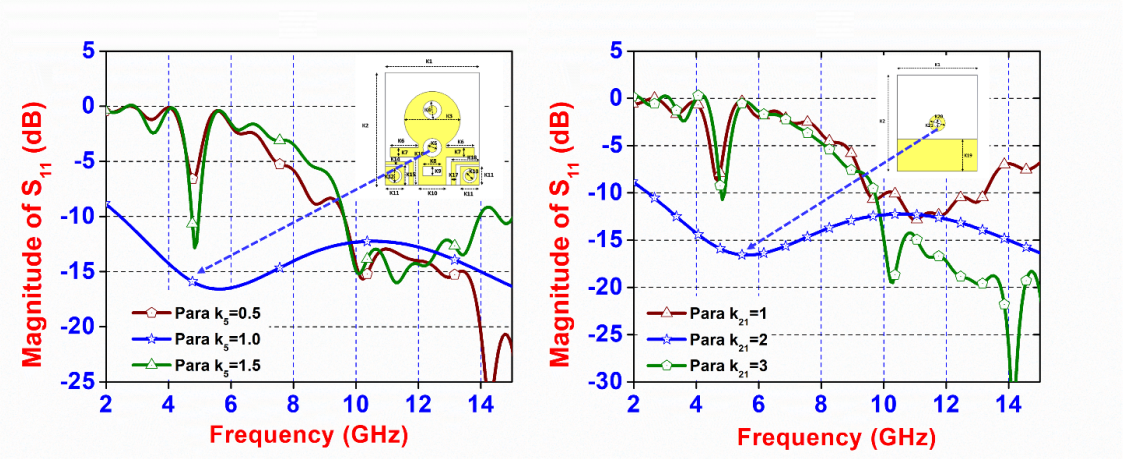

(a) (b)

FIGURE 7. Magnitude of (S_{11}) response showing the effect of (a) feed-slot parameter K_5 and (b) defected ground parameter K_{21}.

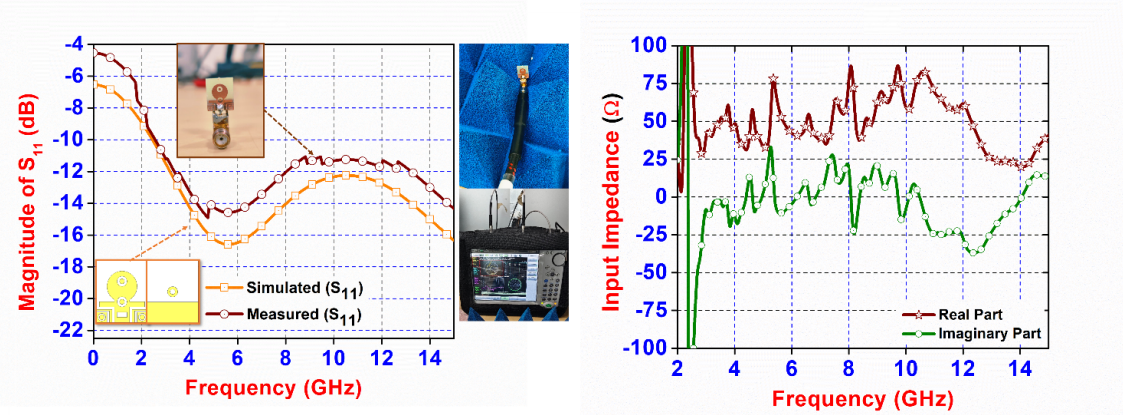

(a) (b)

FIGURE 8. (a) Simulated and measured magnitude of (S_{11}) of the fabricated antenna. (b) Real and imaginary parts.

15 GHz with reflection coefficients below −10 dB. The antenna design was first simulated and optimized using CST Microwave Studio, after which it was fabricated on an FR-4 substrate in an antenna laboratory. The experimental characterization was performed using a vector network analyzer (VNA) inside an anechoic chamber. The measured response closely followed the simulated trend, confirming the accuracy of the design and fabrication process. The small deviations are mainly attributed to fabrication tolerances, connector losses, and practical measurement conditions.

Figure 8(b) shows the input impedance variation of the antenna in terms of its real and imaginary components. The real part of the impedance remains close to 50 Ω over most of the operating band, indicating an efficient power transfer from the feed line to the antenna. At the same time, the imaginary component stays near zero, alternating slightly between inductive and capacitive behavior across the frequency range. This balanced impedance response ensures minimal reflections and a stable wide-band performance, further validating the suitability of the antenna for practical broadband wireless applications.

Figure 9 shows the co-polarized radiation patterns of the proposed antenna in the principal planes at 6 GHz and 14 GHz obtained from both simulation and measurement. At 6 GHz, the H-plane (a) presents an almost omnidirectional response, indicating uniform radiation around the antenna, whereas the E-plane (b) exhibits a bidirectional pattern with two dominant lobes and a clear null, confirming the excitation of the fundamental resonant mode. The measured patterns closely follow the simulated curves with only slight variations due to fabrication tolerance and measurement setup. At 14 GHz, the radiation becomes more directive because of higher-order mode excitation; however, the H-plane (c) still retains a quasi-omnidirectional characteristic, while the E-plane (d) shows multiple lobes with a dominant main beam. Overall, the strong agreement between simulated and measured results in all four cases confirms stable co-polarized radiation and reliable wide-band performance of the antenna.

Figure 10 presents the cross-polarized radiation patterns of the proposed antenna in both principal planes at 6 GHz and 14 GHz from simulation and measurement. At 6 GHz, the H-plane (E) shows very weak cross-polarized components with only small localized lobes, indicating strong suppression of the undesired polarization. The E-plane (F) exhibits slightly higher levels, but the radiation remains confined to limited directions and is still much lower than the co-polarized field. The measured curves closely follow the simulated responses. At

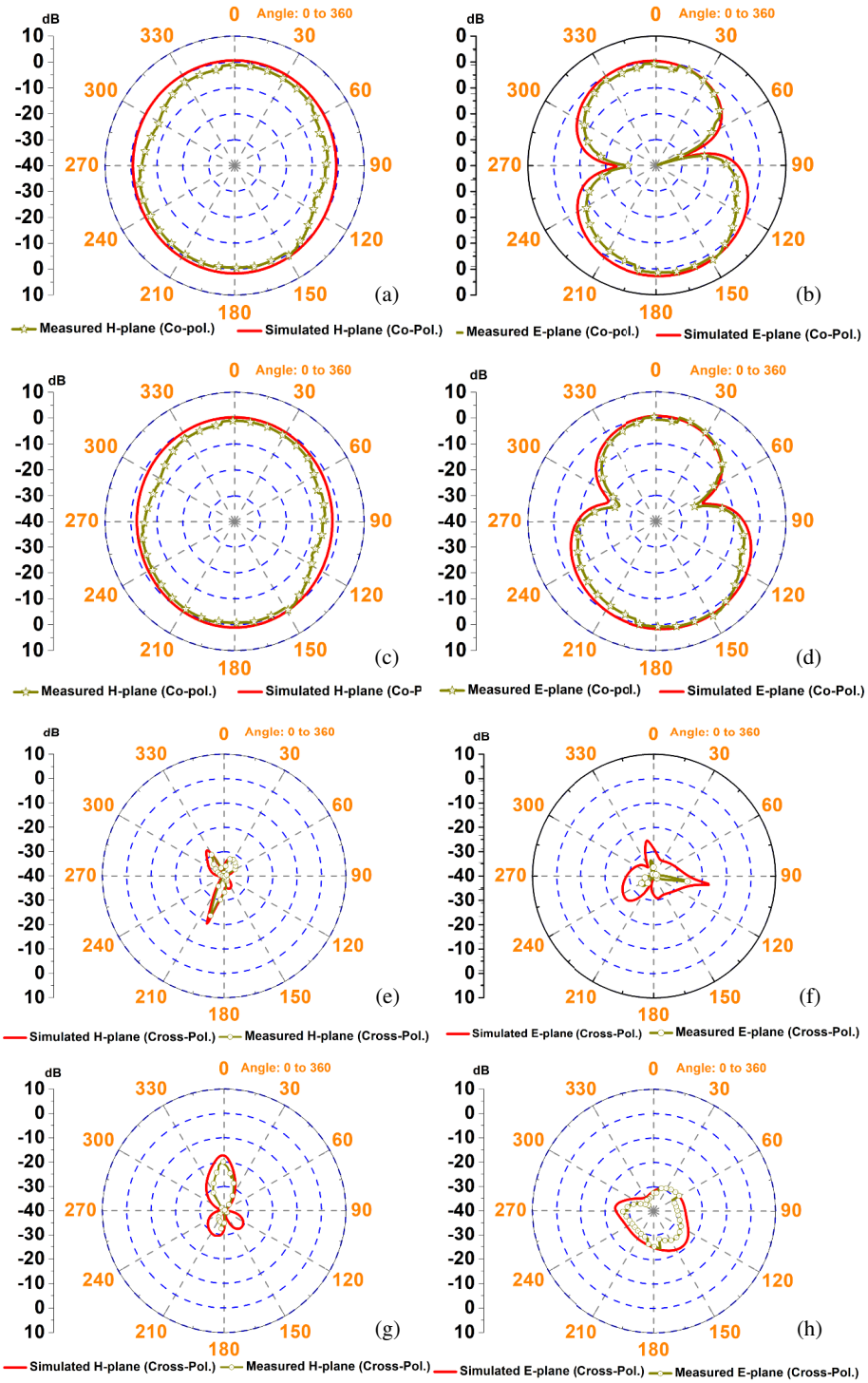

FIGURE 9. Co-polarized radiation patterns of the proposed antenna obtained from simulation and measurement: (a) H-plane at 6 GHz, (b) E-plane at 6 GHz, (c) H-plane at 14 GHz, and (d) E-plane at 14 GHz (magnitude in dB versus angle in degrees).

14 GHz, additional variations appear because of higher-order mode excitation; however, the H-plane (G) continues to maintain low cross-polarized magnitude, while the E-plane (H) displays a few directional lobes of moderate strength. Overall, the antenna maintains low cross-polarization over the operating band, confirming good polarization purity and stable radiation performance.

Figure 11 illustrates the surface current distribution on the proposed antenna at two representative frequencies, highlighting the active radiating regions and current paths responsible for the radiation. At 6 GHz (a), the surface current is primarily concentrated along the outer edges of the main circular radiator and feed transition region, forming a dominant current loop associated with the lower resonant mode. A moderate current density

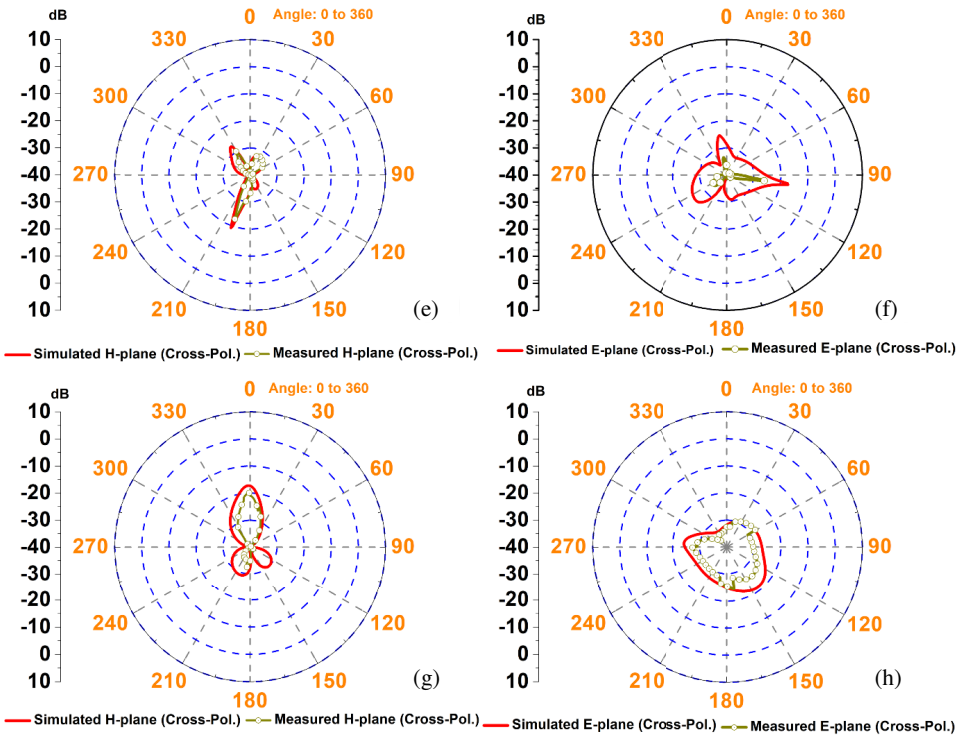

FIGURE 10. Cross-polarized radiation patterns of the proposed antenna obtained from simulation and measurement: (e) H-plane at 6 GHz, (f) E-plane at 6 GHz, (g) H-plane at 14 GHz, and (h) E-plane at 14 GHz (magnitude in dB versus angle in degrees).

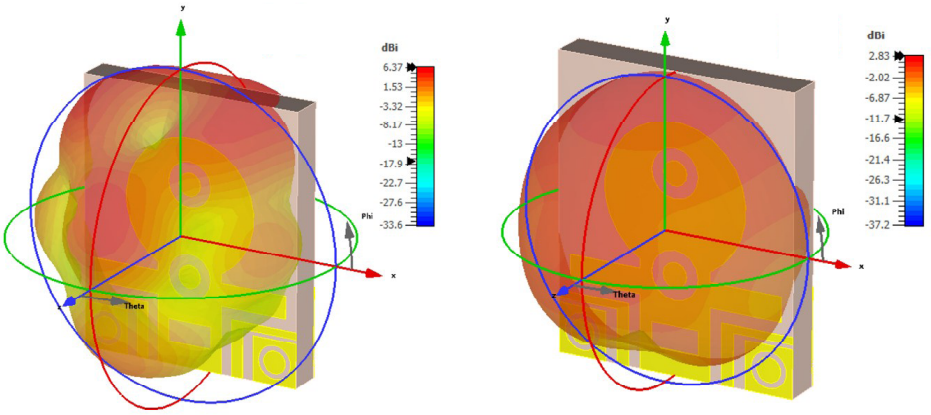

FIGURE 11. Surface current distribution at (a) 6 GHz and (b) 14 GHz.

was also observed on the partial ground plane, indicating strong coupling between the radiator and the ground. The current flow remained relatively uniform and smoothly distributed, confirming that the fundamental resonance was governed mainly by the main patch geometry and feed structure.

At 14 GHz (b), the surface current intensity increased and became more localized, particularly around the inner circular slot, lower stepped arms, and slot edges. The current paths were shorter and more complex, indicating the excitation of higher-order resonant modes in the upper frequency band. Strong currents were also observed around the defected ground and slot regions, demonstrating their roles in bandwidth enhancement and impedance tuning. The contrast between the current distributions at 6 GHz and 14 GHz clearly explains the wide-band behavior of the antenna, where the main patch dominates the lower-frequency radiation, whereas the slots and stepped structures contribute significantly at higher frequencies.

Figure 12 illustrates the three-dimensional radiation characteristics of the proposed antenna at 6 GHz and 14 GHz. At 6 GHz, the antenna demonstrates a wide and nearly omnidirectional radiation pattern with a maximum realized gain of about 6.37 dBi, indicating smooth field distribution, stable radiation behavior, and efficient power radiation at the lower end of the operating band. In contrast, at 14 GHz, the radiation pattern becomes more directive, with radiated energy concentrated along specific directions. The gain at this frequency increases from

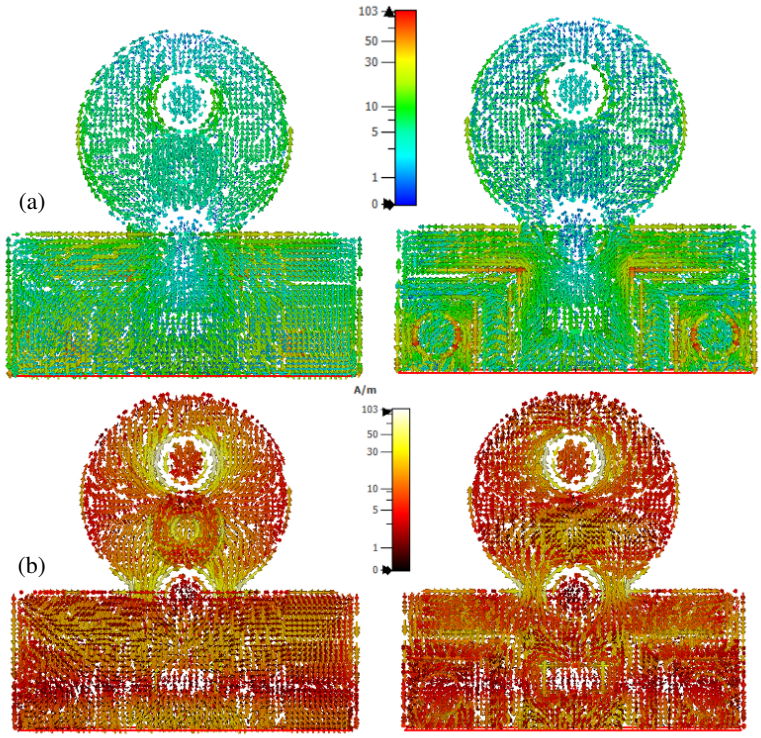

FIGURE 12. Three-dimensional radiation patterns at (a) 6 GHz and (b) 14 GHz.

TABLE 3. Comparison of the proposed antenna with reported planar antennas.

Ref. No.	Antenna Type / Technique	Size (mm^3)	Bandwidth (GHz)	Peak Gain (dB)	Efficiency (%)
[2]	Broadband microstrip antenna for 5G	20×18×1.6	26–30	6.1	85
[4]	U-slot dual-beam microstrip antenna	45×45×1.6	3.1–6.2	7.2	88
[6]	Wide-band planar antenna	35×30×1.6	2.5–10.5	4.8	82
[8]	Compact microstrip antenna for 5G	18×16×1.6	24–29	5.5	80
[12]	Slot-cut rectangular patch antenna	40×30×1.6	3–9	4.2	78
[13]	Miniaturized UWB antenna with partial ground	28×24×1.6	3.1–10.6	5.0	84
[15]	S/C/Xband compact antenna	22×20×1.6	2–12	6.0	86
[18]	Circular compact UWB antenna	25×22×1.6	3–11	5.6	87
This Work	Slot-loaded circular planar antenna with DGS	10×12×1.5	2.4–15	6.37	89

approximately 2.83 dBi to a peak value of around 4 dBi, which is lower than that at 6 GHz due to the excitation of higher-order modes at higher frequencies. These modes lead to increased field cancellation and mild pattern distortion, resulting in reduced gain. Nevertheless, the main radiation lobe remains dominant with only minor side lobes, confirming that the antenna preserves effective radiation performance and acceptable directivity across the upper-frequency range.

From Table 3, it is evident that the proposed antenna offers a significantly reduced footprint while achieving wider impedance bandwidth and higher radiation efficiency than most reported designs. The integration of slot loading, stepped feed, and defective ground structure enables broadband performance without compromising compactness, making the antenna well suited for modern wide-band wireless applications.

8. CONCLUSION

In this article, a slot-loading-enabled compact UWB planar antenna with circuit-backed modelling is presented for defense communication applications. The antenna integrates a modified circular radiator, slot loading, a stepped feed network, and a defected ground plane to realize wide-band impedance matching from 2.4 to 15 GHz within a compact footprint of $10\times12\times1.5\,mm^3$. The design achieves a maximum gain of 6.37 dB and a radiation efficiency of approximately 89%, while maintaining stable radiation patterns with dominant co-polarization and suppressed cross-polarization across the operating band. An electrical equivalent circuit model was developed to explain the multi-resonant behavior and provide an efficient circuit-level validation of the antenna performance. The close agreement between the simulated and measured

results confirmed the reliability of the proposed design. Owing to its compact size, wide bandwidth, high efficiency, and robust polarization characteristics, the antenna is well-suited for UWB defense and tactical wireless communication systems.

REFERENCES

[1] Mishra, B., R. K. Verma, R. K. Singh, *et al.*, "A review on microstrip patch antenna parameters of different geometry and bandwidth enhancement techniques," *International Journal of Microwave and Wireless Technologies*, Vol. 14, No. 5, 652–673, 2022.

[2] Przesmycki, R., M. Bugaj, and L. Nowosielski, "Broadband microstrip antenna for 5G wireless systems operating at 28 GHz," *Electronics*, Vol. 10, No. 1, 1, 2021.

[3] Imran, D., M. M. Farooqi, M. I. Khattak, Z. Ullah, M. I. Khan, M. A. Khattak, and H. Dar, "Millimeter wave microstrip patch antenna for 5G mobile communication," in *2018 International Conference on Engineering and Emerging Technologies (ICEET)*, 1–6, Lahore, Pakistan, 2018.

[4] Khidre, A., K.-F. Lee, A. Z. Elsherbeni, and F. Yang, "Wide band dual-beam U-slot microstrip antenna," *IEEE Transactions on Antennas and Propagation*, Vol. 61, No. 3, 1415–1418, 2013.

[5] Baudha, S., K. Kapoor, and M. V. Yadav, "U-shaped microstrip patch antenna with partial ground plane for mobile satellite services (MSS)," in *2019 URSI Asia-Pacific Radio Science Conference (AP-RASC)*, 1–5, New Delhi, India, 2019.

[6] Kurniawan, A. and S. Mukhlishin, "Wideband antenna design and fabrication for modern wireless communications systems," *Procedia Technology*, Vol. 11, 348–353, 2013.

[7] Ghosh, A., S. K. Ghosh, D. Ghosh, and S. Chattopadhyay, "Improved polarization purity for circular microstrip antenna with defected patch surface," *International Journal of Microwave and Wireless Technologies*, Vol. 8, No. 1, 89–94, 2016.

[8] Verma, S., L. Mahajan, R. Kumar, H. S. Saini, and N. Kumar, "A small microstrip patch antenna for future 5G applications," in *2016 5th International Conference on Reliability, Infocom Technologies and Optimization (Trends and Future Directions) (ICRITO)*, 460–463, Noida, India, 2016.

[9] Akyildiz, I. F., C. Han, and S. Nie, "Combating the distance problem in the millimeter wave and terahertz frequency bands," *IEEE Communications Magazine*, Vol. 56, No. 6, 102–108, 2018.

[10] Akyildiz, I. F., J. M. Jornet, and C. Han, "Terahertz band: Next frontier for wireless communications," *Physical Communication*, Vol. 12, 16–32, 2014.

[11] Han, C. and Y. Chen, "Propagation modeling for wireless communications in the terahertz band," *IEEE Communications Magazine*, Vol. 56, No. 6, 96–101, 2018.

[12] Deshmukh, A. A., D. Singh, P. Zaveri, M. Gala, and K. P. Ray, "Broadband slot cut rectangular microstrip antenna," *Procedia Computer Science*, Vol. 93, 53–59, 2016.

[13] Hota, S., M. V. Yadav, S. Baudha, and B. B. Mangaraj, "Miniaturized planar ultra-wideband patch antenna with semi-circular slot partial ground plane," in *2019 IEEE Indian Conference on Antennas and Propogation (InCAP)*, 1–4, Ahmedabad, India, 2019.

[14] Baudha, S., H. Garg, and M. V. Yadav, "Dumbbell shaped microstrip broadband antenna," *Journal of Microwaves, Optoelectronics and Electromagnetic Applications*, Vol. 18, No. 1, 33–42, 2019.

[15] Yadav, M. V., S. V. Yadav, T. Ali, S. K. K. Dash, N. T. Hegde, and V. G. Nair, "A cutting-edge S/C/X band antenna for 5G and beyond application," *AIP Advances*, Vol. 13, No. 10, 105123, 2023.

[16] Mazinani, S. M. and H. R. Hassani, "A novel broadband plate-loaded planar monopole antenna," *IEEE Antennas and Wireless Propagation Letters*, Vol. 8, 1123–1126, 2009.

[17] Kim, G.-H. and T.-Y. Yun, "Compact ultrawideband monopole antenna with an inverted-l-shaped coupled strip," *IEEE Antennas and Wireless Propagation Letters*, Vol. 12, 1291–1294, 2013.

[18] Yadav, S. V., M. V. Yadav, T. Ali, S. K. K. Dash, N. T. Hegde, and V. G. Nair, "A circular compact ultra-wideband antenna for 5G microwave applications," *TELKOMNIKA (Telecommunication Computing Electronics and Control)*, Vol. 22, No. 3, 556–566, 2024.

[19] Gupta, R., M. V. Yadav, and S. V. Yadav, "TL-shaped circular parasitic compact planar antenna for 5G microwave applications," in *Innovations in Electrical and Electronic Engineering*, Vol. 1109, 507–515, Springer, Singapore, 2023.